

AD-A166 149

SECU

DTIC ELECTE S APR 1 1988 D

REPORT DOCUMENTATION PAGE

1a. REPORT SECURITY CLASSIFICATION <b>UNCLASSIFIED</b>		1b. RESTRICTIVE MARKINGS	
2a. SECURITY CLASSIFICATION AUTHORITY		3. DISTRIBUTION/AVAILABILITY OF REPORT Approved for public release; distribution unlimited.	
2b. DECLASSIFICATION/DOWNGRADING SCHEDULE		4. PERFORMING ORGANIZATION REPORT NUMBER(S) <del>149620-83-C-0025</del>	
4. PERFORMING ORGANIZATION REPORT NUMBER(S)		5. MONITORING ORGANIZATION REPORT NUMBER(S) <del>149620-83-C-0025</del> <b>86-0053</b>	
6a. NAME OF PERFORMING ORGANIZATION California Institute of Tech. Seismological Laboratory	6b. OFFICE SYMBOL (If applicable)	7a. NAME OF MONITORING ORGANIZATION Air Force Office of Scientific Research	
6c. ADDRESS (City, State and ZIP Code) Pasadena, California 91125		7b. ADDRESS (City, State and ZIP Code) Bolling Air Force Base Washington D. C. 20332 <b>-6448</b>	
8a. NAME OF FUNDING/SPONSORING ORGANIZATION <b>AFOSR</b>	8b. OFFICE SYMBOL (If applicable) <b>ND</b>	9. PROCUREMENT INSTRUMENT IDENTIFICATION NUMBER <b>F49620-83-C-0025</b>	
8c. ADDRESS (City, State and ZIP Code) (DOD) <b>AFOSR Bldg 410 Bolling AFB, DC 00338-6448</b>		10. SOURCE OF FUNDING NOS.	
11. TITLE (Include Security Classification) Body and Surface Wave Modeling of Observed Seismic Events		PROGRAM ELEMENT NO. <b>61102F</b>	TASK NO. <b>2309</b>
12. PERSONAL AUTHOR(S) David G. Harkrider, Donald V. Helmberger and Robert W. Clayton		WORK UNIT NO. <b>A1</b>	WORK UNIT NO. <b>N/A</b>
13a. TYPE OF REPORT Final Report	13b. TIME COVERED FROM <b>5/1/84</b> TO <b>12/15/84</b>	14. DATE OF REPORT (Yr., Mo., Day) 1/22/86	15. PAGE COUNT 72
16. SUPPLEMENTARY NOTATION			
17. COSATI CODES		18. SUBJECT TERMS (Continue on reverse if necessary and identify by block number)	
FIELD	GROUP	Lg, continent-ocean transitions, long-period body waves, constraints on local mechanisms, S and SS across transitions	
	SUB. GR.		
19. ABSTRACT (Continue on reverse if necessary and identify by block number)			
<p>The research performed under the contract, during the period 1 May 1984 through 15 December 1984, can be divided into three major topics; modeling Lg propagation across regional transition zones, the use of long period body waves to constrain focal mechanism orientation, and WKBJ modeling of S and SS to investigate the nature of the boundary between a tectonic and shield region.</p> <p>In Section II, results of modeling Lg waves crossing continental margins by combining analytic with finite element calculations are presented. The accuracy of the formulation is tested by using a layer-over-halfspace model for which a solution can be independently determined using conventional mode sum calculations. This test case is also used to illustrate the efficiency of an absorbing boundary condition designed to reduce com-</p>			
20. DISTRIBUTION/AVAILABILITY OF ABSTRACT UNCLASSIFIED/UNLIMITED <input checked="" type="checkbox"/> SAME AS RPT. <input type="checkbox"/> DTIC USERS <input type="checkbox"/>		21. ABSTRACT SECURITY CLASSIFICATION <b>UNCLASSIFIED</b>	
22a. NAME OF RESPONSIBLE INDIVIDUAL <b>RAIMON E. KELLEY</b>		22b. TELEPHONE NUMBER (Include Area Code)	22c. OFFICE SYMBOL <b>NP</b>

DTIC FILE COPY

86 4 1 019

FINAL TECHNICAL REPORT  
1 May 1984 - 15 December 1984

ARPA Order No.: 4397/3  
Program Code: 3D60  
Name of Contractor: California Institute of Technology  
Effective Date of Contract: 1 November 1982  
Contract Expiration Date: 15 December 1984  
Amount of Contract: \$435,000  
Contract Number: F49620-83-C-0025  
Principal Investigators: David G. Harkrider  
(818) 356-6910  
Donald V. Helmberger  
(818) 356-6998  
Robert W. Clayton  
(818) 356-6909  
Program Manager and Telephone Number: William J. Best  
(202) 767-4904  
Short Title of Work: Body and Surface Wave Modeling  
of Observed Seismic Events

The views and conclusions contained in this document are those of the authors and should not be interpreted as necessarily representing the official policies, either expressed or implied, of the Defense Advanced Research Projects Agency of the U.S. Government

Sponsored by

Advanced Research Projects Agency (DOD)  
ARPA Order No. 4397/3

Monitored by AFOSR under Contract No. F49620-83-C-0025

Seismological Laboratory  
Division of Geological and Planetary Sciences  
California Institute of Technology  
Pasadena, California 91125

AIR FORCE OFFICE OF SCIENTIFIC RESEARCH (AFSC)

NOTICE OF TRANSMITTAL TO DTIC

This technical report has been reviewed and is approved for public release INW APR 190-12.

Distribution is unlimited.

MATTHEW J. KEMPNER

Chief, Technical Information Division

TABLE OF CONTENTS

	<u>Page</u>
Summary. . . . .	I-1
Modeling Lg wave propagation in laterally heterogeneous media.	II-1
A body-wave analysis of the 1966 Gisborne, New Zealand, Earthquake. . . . .	III-1
Upper-mantle cross section from California to Greenland . . .	IV-1



Accession For	
NTS GR&I	<input checked="" type="checkbox"/>
NTS TAB	<input type="checkbox"/>
Unannounced	<input type="checkbox"/>
Subscription	<input type="checkbox"/>
By	
Distribution/	
Availability Codes	
Dist	Avail and/or Special
A1	

## I. Summary

The research performed under the contract, during the period 1 May 1984 through 15 December 1984, can be divided into three major topics; modeling Lg propagation across regional transition zones, the use of long period body waves to constrain focal mechanism orientation, and WKB modeling of S and SS to investigate the nature of the boundary between a tectonic and shield region.

In Section II, results of modeling Lg waves crossing continental margins by combining analytic with finite element calculations are presented. The accuracy of the formulation is tested by using a layer-over-halfspace model for which a solution can be independently determined using conventional mode sum calculations. This test case is also used to illustrate the efficiency of an absorbing boundary condition designed to reduce computation time. In the modeling of transition regions, the decrease in crustal thickness from continents to oceans focuses seismic energy. This results in surface amplitudes that are 50% larger in the oceanic crust near the end of the transition than those in the adjacent continent. However, the amplitude of the Lg waves rapidly attenuates as they propagate to larger distances in the oceanic crust. Conversely, amplitudes are reduced when the Lg wavetrain passes through the transition from ocean to continent because energy disperses into the thickening crustal layer.

In Section III, a body-wave analysis of the 1966 Gisborne, New Zealand, earthquake is given. The  $M_L = 6.2$  event occurred along the east coast of the North Island. Modeling of P and S body waves shows that the focal mechanism of this event is consistent with the northwestward thrusting of the Pacific Plate beneath North Island ( $\phi = 249^\circ$ ,  $\delta = 25^\circ$  and  $\lambda = 131^\circ$ ). The focal depth is constrained to 18 km, significantly less than the values of 25 to 30 km computed from local network data. Estimates of scalar moment, source duration and stress-drop for the event are  $4 \times 10^{24}$  dyne-cm, 2 to 3 seconds, and 20 to 120 bars respectively. Cross-correlation errors of synthetic to observed waveforms were computed for all possible P and T axis locations and slip vector orientations and contoured on a projection of the focal sphere. The error contour at which the synthetic waveforms distinctly diverged from the observed waveforms was established by eye. The procedure shows that the analysis of long-period waves, at least in this case, provides much better constraint on focal mechanism orientation than does first motion data alone.

In Section IV, results are presented of modeling observations of S, SS, and SSS where the event occurs near tectonic margins and are recorded on stable continents. The modeling for laterally varying structure is essentially along a profile from California to Greenland. The models are allowed to be locally dipping with the lithosphere thickening with age at the expense of a dwindling low velocity zone. Lateral variation does not appear to be required for depths greater than 400 km along this particular profile. The best fitting model has a large increase in lithospheric thickness near the Rocky Mountain Front, roughly an increase in 75 km over a horizontal distance of 400 km or less. The low velocity zone, with a velocity of 4.4 km/sec, is replaced by a much faster upper

300 km with velocities near 4.7 km/sec or a 7% overall increase. The one-way travel time jumps by roughly 4 secs across this boundary which compares reasonably well with the direct S residuals obtained from deep earthquake data although the latter data show large scatter.

## II. Modeling Lg wave propagation in laterally heterogeneous media.

Janice Regan

### SUMMARY

We have developed finite element forms of the seismic Representation Theorem (RT) to model Lg waves crossing continental margins. We have verified the accuracy of this formulation using a layer-over-halfspace model for which a solution can be independently determined using conventional mode sum calculations. We also used this test case to illustrate the efficiency of an absorbing boundary condition designed to reduce computation time. In the modeling of transition regions, the decrease in crustal thickness from continents to oceans focuses seismic energy. This results in surface amplitudes that are 50% larger in the oceanic crust near the end of the transition than those in the adjacent continent. However, the amplitude of the Lg waves rapidly attenuates as they propagate to larger distances in the oceanic crust. Conversely, amplitudes are reduced when the Lg wavetrain passes through the transition from ocean to continent because energy disperses into the thickening crustal layer.

### INTRODUCTION

The principal advantage of our RT technique for propagating Lg waves is that it enables us to perform the calculations for mode sums. We are not restricted to mode by mode calculations through the transition region as in previous studies. In the results reported here, Lg is represented by the fundamental and first 5 higher SH modes. These 6 modes are then simultaneously propagated through the Finite Element (FE) grid representing the transition region of interest. A further advantage coupling is that the FE calculations are driven by specifying the displacement time histories at a column of nodes which represents the boundary between the laterally homogeneous region and the transition zone. These time histories can be calculated using standard techniques when the source is separated from the margin by long continental paths. Alternatively, they can be input from other FE calculations, as in the case of the continent-ocean-continent transition discussed below. We should point out however that our technique is only valid for waves propagating at normal incidence.

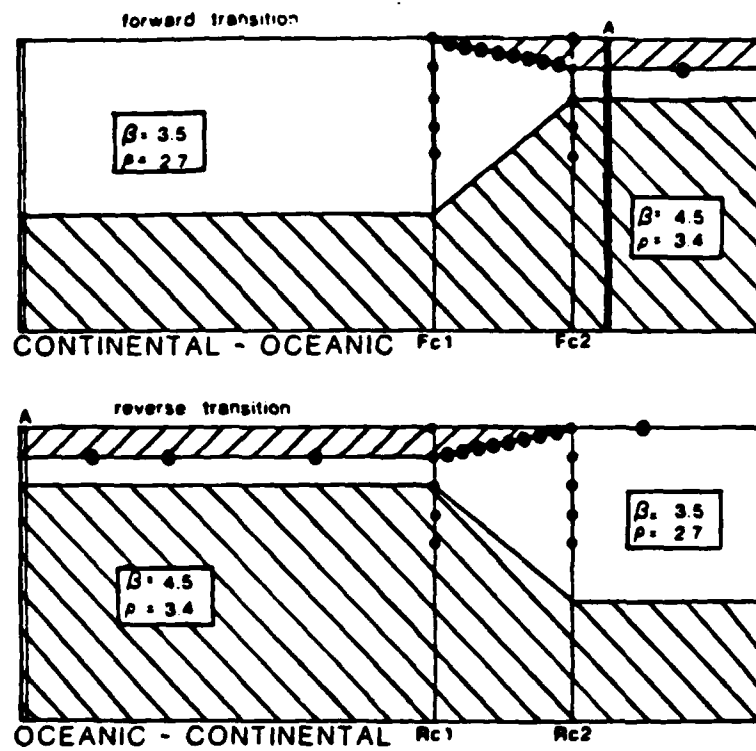
absorbing were also calculated using the short grid for the FE portion of the calculation. However, in this case the absorbing BC was imposed at the dotted vertical line in Figure 1a. The results show that the absorbing BC is very efficient for Lg mode sum input.

Reflections from the bottom edge of the grid should also be considered. In the case of an SH pulse propagating in a half-space reflections from the bottom of the grid also introduce difficulties. However, for the case of Lg mode sums propagating in a layer over a half-space, the Lg wave interacts predominantly with the real boundary between the layer and the half-space. Introducing absorbing BC's on the bottom of the grid makes no perceptible difference in the results. Since including the BC slightly increases the number of operations required at each boundary node at each time step, the bottom edge of the grid is not constrained in any of the examples described here.

The FE grids used to study the propagation of an Lg wave along a continental to oceanic to continental path are shown in Figure 2a. The forward transition that takes the energy across a continental to oceanic transition region is modeled as a smooth thinning of the crustal layer and a gradual introduction of a water layer over a distance of twenty kilometers. The pair of vertical lines at the left end of the grid represent nodes constrained to move with the input Lg displacement histories. The 2 vertical lines labeled Fc1 and Fc2 show receiver sections used to determine the effect of the transition on the distribution of energy with depth. The pair of vertical lines labeled A are nodes for which displacement histories are recorded to use as input to the reverse transition. The reverse transition grid takes the wave across an oceanic to continental transition region. This transition is modeled as a smooth thickening of crust and thinning of the water layer over a distance of twenty kilometers. The pair of vertical lines at the left end of the grid are the nodes constrained to move with the Lg displacement histories recorded at the column marked A in the forward transition grid. The 2 vertical lines marked Rc1 and Rc2 show receiver sections used to determine the effect of the transition on the energy distribution with depth. Dots on Fc1, Fc2, Rc1, and Rc2 indicate positions of receivers for which displacement histories are illustrated in Figure 2b. Open circles refer to nodes for which displacement histories are plotted in Figure 2c.

The passage of the Lg wave through the transition region effects the distribution of energy with depth. The energy impinging on the crust/water sloping boundary is mostly reflected. Since no energy is transmitted into the water layer, the remaining energy is focussed along the sloping boundary into the oceanic crustal layer. This can be seen from Figures 1b and 2b. Comparing the seismograms in row Fc1 of Figure 2b and the synthetic traces for a layer over a half-space shown in Figure 1b, the difference in wave shape indicates interference of a reflected wave and the propagating Lg.

a)



b)

depth sections of displacement histories

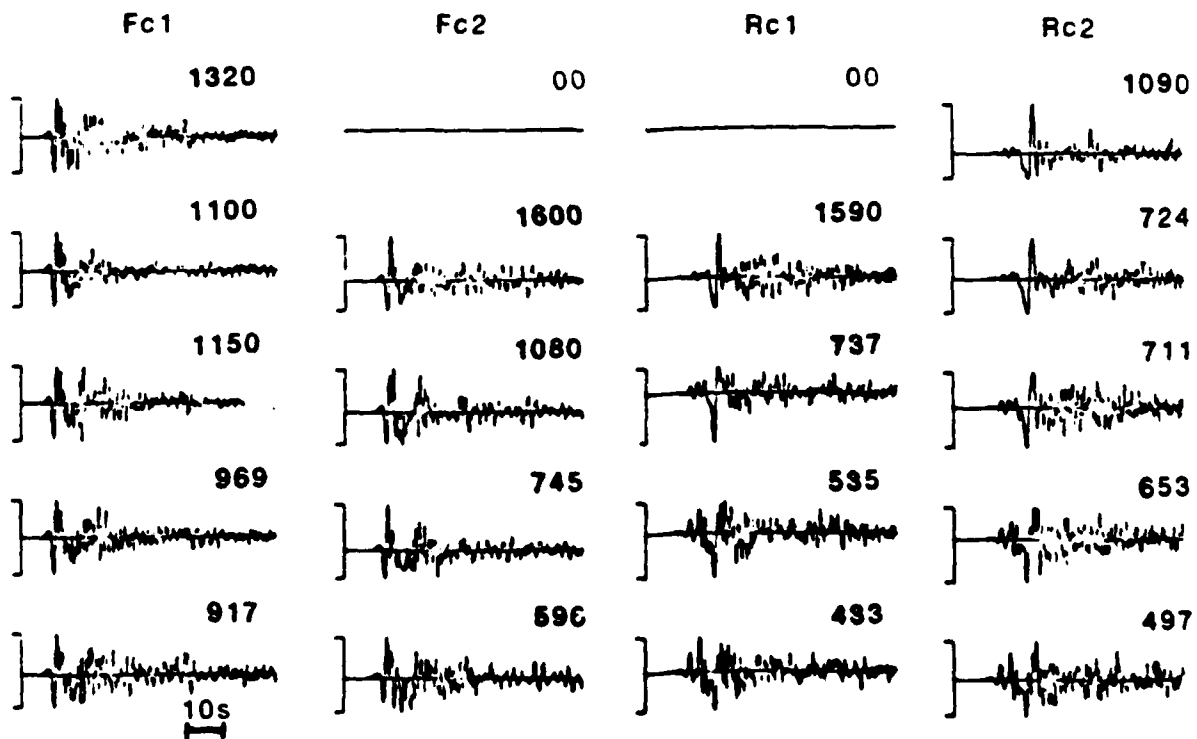


Figure 2



### III. A Body-Wave Analysis of the 1966 Gisborne, New Zealand, Earthquake.

*Terry H. Webb\*, S. G. Wesnousky and Donald V. Helmberger.*

Seismological Laboratory,  
California Institute of Technology,  
Pasadena, California 91125.

#### Abstract

The  $M_L = 6.2$  Gisborne earthquake of March 4, 1966 occurred along the East Coast of the North Island, New Zealand. Modeling of P and S body waves shows that the focal mechanism of this event is consistent with northwestward thrusting of the Pacific Plate beneath the North Island ( $\phi=249^\circ, \delta=25^\circ$  and  $\lambda=131^\circ$ ). The focal depth is constrained to 18 km, significantly less than the values of 25 to 30 km computed from local network data. Estimates of the scalar moment, source duration and stress-drop for the event are  $4 \times 10^{24}$  dyne-cm, 2 to 3 seconds, and 20 to 120 bars respectively. Cross-correlation errors of synthetic to observed waveforms were computed for all possible P and T axis locations and slip vector orientations and contoured on a projection of the focal sphere. The error contour at which the synthetic waveforms distinctly diverged from the observed waveforms was established by eye. The procedure shows that the analysis of long-period body waves, at least in this case, provides much better constraint on focal mechanism orientation than does first motion data alone.

---

\*Now at: Geophysics Division, D.S.I.R., P.O. Box 1320, Wellington, New Zealand.

Recent reanalysis of the New Zealand network data does, however, show the depth of the earthquake to be well-constrained at 25 to 30 km (E. G. C. Smith, personal communication 1984).

#### Teleseismic Data

The WWSSN stations that recorded P and S waves for the Gisborne earthquake are shown in Figure 2. The azimuthal distribution of stations recording the event is poor, primarily due to the relatively small size of the event and the wide expanse of the Pacific Ocean which lies to the north, east and south of New Zealand. In summary, 8 reliable P waveforms and 2 SH waveforms were recovered from the WWSSN library. The P-waves are quite similar to within the noise level which reflects their close spatial distribution on the focal sphere. Some differences, such as the amplitude of the clear second arrival and of the final backswing, are not consistent with relative station location, so probably do not reflect properties of the source. Interestingly, none of the stations that recorded P-waves showed evidence of SH energy, possibly a result of being situated near a S-wave node. Although TAU ( $\Delta=23.5^\circ$ ) and RIV ( $\Delta=22.0^\circ$ ) recorded tangential motion, the waveforms were dominated by Love waves and were consequently not useful. It should also be noted that the TAU P-wave has been used without modeling the possible effects of a triplication. The similarity of the P waveform recorded at TAU to P waveforms recorded nearby on the focal sphere (Figure 2) suggests that the TAU P waveform has not been complicated by triplication effects. The TAU waveform is actually the radial component, as the vertical one was not recorded.

main effect of lowering the surface velocities was to reduce the size of the sP phase.

### Results

Synthetic waveforms for the best-fitting solution ( $\varphi=249^\circ$ ,  $\delta=25^\circ$  and  $\lambda=131^\circ$ ) are compared to the observed waveforms in Figure 2. All of the P-wave data show a prominent depth phase about 10 seconds after the first arrival. Some difficulty was initially experienced in deciding whether this was the phase pP or sP. As this radically affects the final best-fitting mechanism and our result for the focal depth differs from previous studies, we examine this question in detail. Interpretation of the strong depth phase as pP is consistent with the 25 to 30 km depth determined from regional network data. However, the best-fitting mechanism, assuming a 28 km focal depth produces synthetic waveforms that do not fit well at three stations (GSC, PAS and TAU). Relatively good fits to the data from all stations were achieved if synthetics were made with an 18 km focal depth, which implies that the prominent depth phase is sP, not pP. The synthetics for each depth for two of the sensitive stations, GSC and TAU, are shown in Figure 3. The synthetic SH pulse width for an assumed focal depth of 28 km is wider than that observed at GSC, whereas a good match is obtained when an 18 km depth is used. Since the width of the SH waveform is governed by the S-sS time delay, this provides an unambiguous constraint on the depth. In addition, the choice of an 18 km focal depth provides a superior fit to the TAU waveform compared to that for the 28 km depth. At the greater depth there is a strong trade-off between the TAU P and GSC SH waves becoming nodal.

Further evidence for identifying the prominent depth phase as sP was found by comparing short-period records from the South American stations ARE and PEL, for which there are no long-period data, with short-period records from two stations at opposite azimuths - RAB and SNG. The vertical component waveforms are shown in

A trapezoidal time function of 0.7, 1.0 and 0.7 seconds was used for the synthetics. Other shapes could fit equally well, but the overall source duration was determined to be in the range 2 to 3 seconds. This is within the range of source durations (for an event of this size) for the group of plate boundary events compiled by Liu and Kanamori (1980). Assuming a circular fault, rays leaving at  $45^\circ$  to the normal to the fault plane and, using the formula derived by Geller (1976) and Ebel et al. (1978), we calculated a fault radius of 2.6 to 4.0 km. The stress-drop, calculated from Brune's (1970) circular fault model, is then 20 to 120 bars.

The most subjective part in determining the degree of constraint on the final focal mechanism was in assessing for which values of cross-correlation error the synthetic fits became unacceptable. Once this was established by eye, an algorithm based on the program FOCPLT (Whitcomb, 1973), which tests all possible double couple mechanisms in 3.5 degree steps, was used to determine the cross-correlation errors for all mechanisms, P and T axis locations and slip vector orientations. These could then be contoured to the level of satisfactory fits and could also be compared with similar plots made using the first motion data.

Figure 5 shows the range of possible mechanisms determined from body-wave modelling (A) and first motion data (B), while Figure 6 shows possible slip vector orientations and P and T axis locations corresponding to this range of mechanisms for the event. The dashed curves in Figure 6 show the possible range using first motion data while the solid curves denote the range of acceptable values that produce satisfactory agreement of synthetic and observed waveforms. The body-wave modeling appears to have reduced the uncertainty in slip vector and P and T axis locations by about a factor of two, and is also more reliable since more than just first motions are being matched.

The failure to match the final backswing at four stations (PMG, CTA, HKC and SNG) with the synthetics could suggest some source complexity, such as a second

The possible range of horizontal projections of slip vectors for our solution favour slip in the azimuth range  $265^{\circ}$  to  $335^{\circ}$ . The relative plate motion in this region is directed at an azimuth of  $270^{\circ}$  (Walcott, 1978). Since this is near one extreme of the range of slip vectors, it appears likely that slip occurred more nearly perpendicular to the strike of the Wadati-Benioff zone than the plate motion direction and that the remaining component of plate motion is being accommodated by strike-slip movement in a shear zone further inland, as proposed by Walcott (1978).

#### Conclusions

Analysis of P and S waveforms has allowed us to provide more constraint on the focal mechanism of the 1966 Gisborne earthquake than has previously been afforded by first motion data alone. Similar analysis of other moderately sized earthquakes along the New Zealand plate boundary may help to refine and constrain models of plate motion and deformation.

The preferred strike, dip, rake and depth of the 1966 Gisborne earthquake are  $249^{\circ}$ ,  $25^{\circ}$ ,  $131^{\circ}$  and 18 km, respectively. The simplest interpretation of this earthquake is that it is a typical subduction zone thrust event with a small right-lateral component due to the oblique convergence of the Pacific and Indian plates in this region. There is no evidence from our study to suggest that this region is currently undergoing extension normal to the strike of the subducted plate as suggested by strain data for the period 1931 to 1970 (Walcott, 1978), although there may be a difference between the strain occurring in the upper crust and that occurring near the plate interface. Determination of other reliable earthquake mechanisms can help to clarify these observations by showing whether the Gisborne event occurred during a short period of east-west compression in a region that has apparently otherwise had steady east-west extension in the past 50 years, or whether there is a change in the direction of principal horizontal compression with depth in the crust. It is

**References**

- Adams, R. D. and D. E. Ware (1977). Subcrustal earthquakes beneath New Zealand; locations determined with a laterally inhomogeneous velocity model, N.Z. J. Geol. Geophys. 20, 59-83.
- Brune, J. N. (1970). Tectonic stress and the spectra of seismic shear waves from earthquakes, J. Geophys. Res. 75, 4997-5009.
- Ebel, J. E., L. J. Burdick and G. S. Stewart (1978). The source mechanism of the August 7, 1966 El Golfo earthquake, Bull. Seism. Soc. Am. 68, 1281-1292.
- Futterman, W. I. (1962). Dispersive body waves, J. Geophys. Res. 67, 5279-5291.
- Geller, R. J. (1976). Scaling relations for earthquake source parameters and magnitudes, Bull. Seism. Soc. Am. 66, 1501-1523.
- Hamilton, R. M. (1969). Seismological studies of the Gisborne earthquake sequence, 1966, in Gisborne earthquake New Zealand March 1966, Bull. N.Z. Dept. Sci. & Ind. Res. 194, 7-23.
- Johnson, T and P. Molnar (1972). Focal mechanisms and plate tectonics of the Southwest Pacific, J. Geophys. Res. 77, 5000-5032.
- Langston, C. A. and D. V. Helmberger (1975). A procedure for modelling shallow dislocation sources, Geophys. J. R. astr. Soc. 42, 117-130.
- Liu, H. L. and H. Kanamori (1980). Determination of source parameters of mid-plate earthquakes from the waveforms of body waves, Bull. Seism. Soc. Am. 70, 1989-2004.
- Mellman, G. R., L. J. Burdick and D. V. Helmberger (1975). Determination of source parameters from body wave seismograms, Earthquake Notes 40, 44.
- Reyners, M. (1980). A microearthquake study of the plate boundary, North Island, New Zealand, Geophys. J. R. astr. Soc. 63, 1-22.
- Walcott, R. I. (1978). Geodetic strains and large earthquakes in the axial tectonic

**Table 1. Velocity model for depth determination.**

Depth to top of layer	$V_p$ (km/s)	$V_s$ (km/s)
0	3.00	1.73
2	6.00	3.47
30	6.50	3.70
36	8.10	4.60
41	8.60	4.90

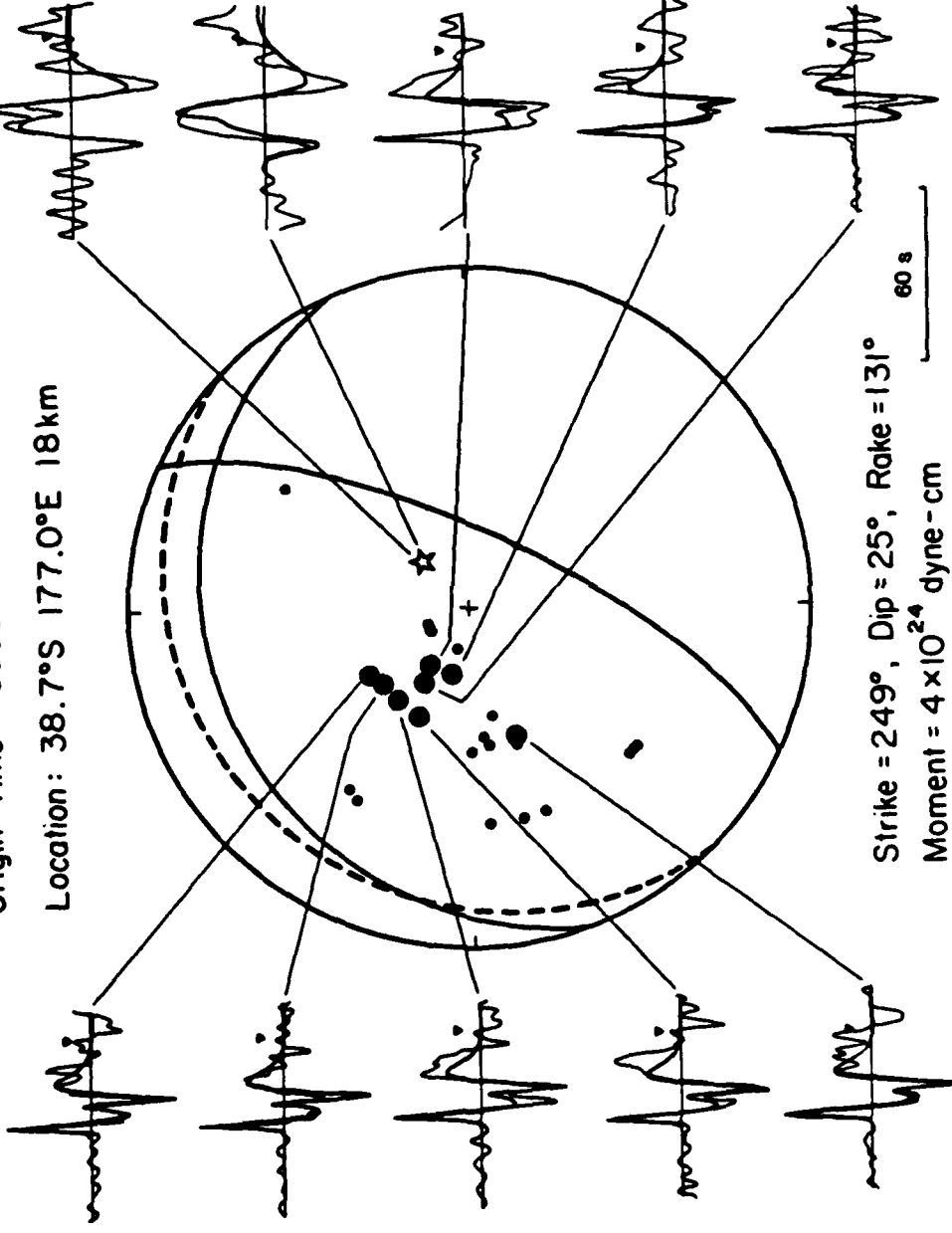
mechanism with  $\varphi=249^\circ$ ,  $\delta=25^\circ$ ,  $\lambda=131^\circ$  and  $H=18$  km, while the bottom traces are for  $\varphi=310^\circ$ ,  $\delta=35^\circ$ ,  $\lambda=105^\circ$  and  $H=28$  km.

Figure 5. Possible range of mechanisms for the body-wave solution (A) and for short-period first motion data (B) on equal-area lower hemisphere projections.

Figure 6. Contours of possible slip vector orientations (A) and P and T axis locations (B) for the body wave data (solid lines) and short-period first motion data (dashed lines). Projections are as in Figure 5.

Origin Time: 660304 2358 56.6

Location: 38.7°S 177.0°E 18km



HNR PZ  
 $A_d = 3.0\text{mm}$   
 $A_s = 4.5\text{mm}$   
 $\Delta = 33.4^\circ$   
 $\phi = 326.1^\circ$

RAB PZ  
 $A_d = 2.4\text{mm}$   
 $A_s = 2.1\text{mm}$   
 $\Delta = 41.6^\circ$   
 $\phi = 319.0^\circ$

PMG PZ  
 $A_d = 2.2\text{mm}$   
 $A_s = 8.9\text{mm}$   
 $\Delta = 40.2^\circ$   
 $\phi = 308.3^\circ$

CTA PZ  
 $A_d = 4.7\text{mm}$   
 $A_s = 10.1\text{mm}$   
 $\Delta = 33.1^\circ$   
 $\phi = 294.9^\circ$

TAU PR  
 $A_d = 1.7\text{mm}$   
 $\Delta = 23.6^\circ$   
 $\phi = 249.8^\circ$

GSC SH  
 $A_d = 2.6\text{mm}$   
 $A_s = 0.9\text{mm}$   
 $\Delta = 95.1^\circ$   
 $\phi = 48.3^\circ$

PAS SH  
 $A_d = 3.3\text{mm}$   
 $\Delta = 93.5^\circ$   
 $\phi = 48.4^\circ$

HKC PZ  
 $A_d = 0.4\text{mm}$   
 $A_s = 1.1\text{mm}$   
 $\Delta = 85.2^\circ$   
 $\phi = 303.3^\circ$

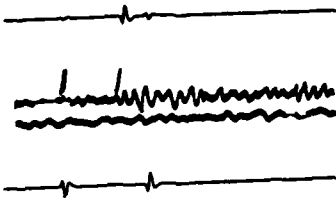
SNG PZ  
 $A_d = 2.6\text{mm}$   
 $A_s = 4.2\text{mm}$   
 $\Delta = 84.7^\circ$   
 $\phi = 283.3^\circ$

DAV PZ  
 $A_d = 6.4\text{mm}$   
 $A_s = 5.5\text{mm}$   
 $\Delta = 66.6^\circ$   
 $\phi = 300.9^\circ$

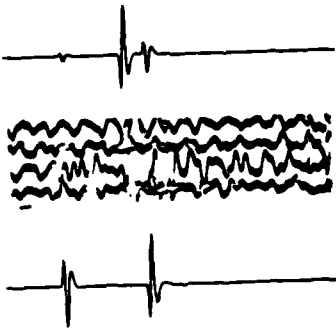
Strike = 249°, Dip = 25°, Rake = 131°  
Moment =  $4 \times 10^{24}$  dyne-cm

60 s

ARE  $\Delta = 95.0^\circ$   
Az = 115.7°



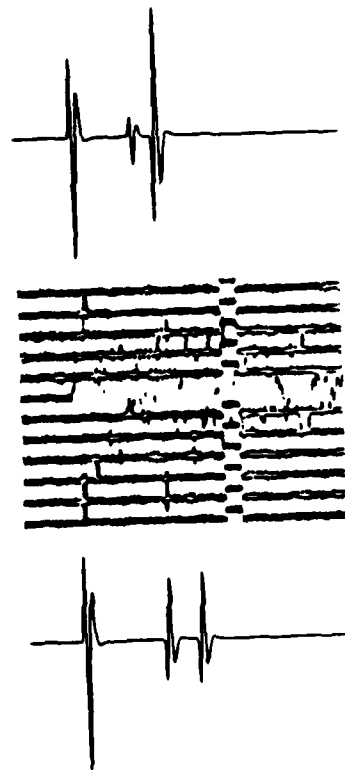
PEL  $\Delta = 84.2^\circ$   
Az = 128.3°

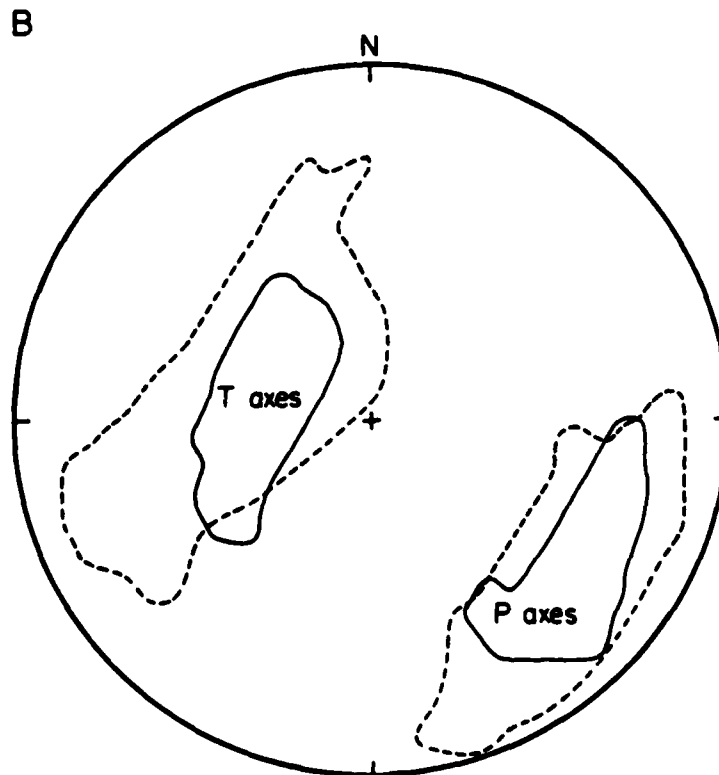
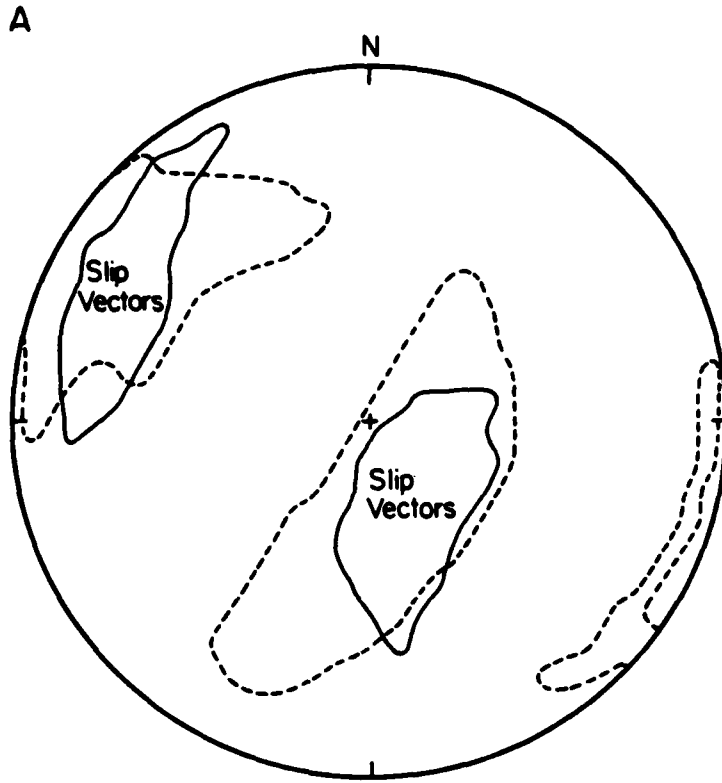


SNG  $\Delta = 84.7^\circ$   
Az = 283.3



RAB  $\Delta = 41.6^\circ$   
Az = 319.0°





#### IV. Upper-Mantle Cross Section From California To Greenland

*Donald V. Helmberger, Gladys Engen and Steve Grand*

*Seismological Laboratory  
California Institute of Technology  
Pasadena, California 91125*

*Revised May 21, 1985*

## 1. Introduction

In a recent paper, (Grand and Helmberger (1984a)), upper mantle models appropriate for pure-path tectonic and shield regions were presented. By analyzing the (SS-S) travel times and waveform information it became apparent that the seismograms could be partitioned into these two groups and interpreted in terms of vertical structure, see Fig. 1. Model SNA was derived from Canadian shield observations but has proven useful in modeling observations from other shields, Rial, et al. (1984). The TNA model appears appropriate for younger oceanic structures and the more tectonic parts of Western North America. Older oceans have a thicker lithosphere approaching the physical characteristics of the shield but conforming to the TNA model with depth as displayed in Fig. 1. Model ATL was derived for the 100 M year old portion of the Western Atlantic, Grand and Helmberger (1984b).

In this paper, we will investigate the nature of the horizontal boundaries that connect the TNA and SNA provinces by modeling the seismograms that sample both areas.

The events used in this study occur along the western seaboard with recordings taken from the WWSSN and CSN stations. The locations of the stations and events are presented in Fig. 2. The events are also listed in Table 1. The reflection points at the free surface for the SS phases occur mostly in the midwest with the bottoming or turning points located in the Western United States and in Eastern Canada. The lateral structure across this region is probably three-dimensional but the general trend is from tectonic to shield. Thus, to simplify a complex situation, we will assume that the data, associated with the station locations displayed in Fig. 2, can be averaged from north to south, i.e. observations at SHA of C2 can be compared to MDS of 05, etc. In general, these seismograms do share common properties as pointed out earlier in Grand and Helmberger (1984a). Figure 3 displays representative seismograms from such paths and synthetics appropriate for the models TNA and SNA. Examining this figure we see that the data are closer to the SNA synthetics in timing but are more similar to the

by the two methods agree about as well as in the flat-layered case, see Grand and Helmberger (1984a). The first arrival in the GRT result, is relatively larger at the nearest distances due to tunnelling through the thin lid. At distances near  $28^\circ$  the second negative peak in the WKB synthetics is too large compared to the GRT results. This arrival is the back branch of the 600 km triplication and such arrivals tend to be too large near the triplication tip, see Burdick and Orcutt (1978) for example. The last arrivals denoted by the arrows are truncation effects. Both can be eliminated or modified by adding more generalized rays, see Helmberger et al (1985). However, we are primarily interested in mapping the position of the triplications and can tolerate some synthetic deficiencies. We will also omit the arrivals guided by the growing lithosphere after giving a brief review of their properties.

A profile of synthetics containing the complete generalized ray set for the linear model is displayed in Fig. 6. As in a recent paper by Grand and Helmberger (1984a) we have broken up the rays into two groups, those that travel in the crust and lid or lithosphere, and those that return from below the low velocity zone, LVZ. All the responses are normalized to the top trace. The short period precursors to the long period Love wave are multiples developing in the growing lid. Upper mantle arrivals become contributors to the complete response at about  $18.2^\circ$  (1800 km) for this particular model. The two sharp spikes occurring in this trace are the onset of the 400 km triplication, essentially S and sS. Rays bottoming between 200 and 300 km produce the main arrivals. Synthetic seismograms assuming a  $t_p^* = 3$  sec and a far-field trapezoidal time history of (1,1,1) are given on the right. We probably over attenuated the lid arrivals in these synthetics since when we can see these precursors on long period observations they are also strong on the short period records implying a high Q.

We do not see precursors for events near the western portion of the United States, see Grand and Helmberger (1984a), although they can be observed in Canada for some events located near the edge of the shield. Since we will be studying mostly western

### Comparison with Observations

Selecting a set of observations to use for comparison with the synthetics discussed in the previous section may seem easy given the large numbers of events available. However, because of radiation pattern effects we may not obtain simple SH pulses along desired paths. SV coupled PL waves make working with rotated records difficult in many situations as pointed out earlier, Helmberger and Engen (1974). Thus, we chose only observations that are relatively naturally rotated or have stations located on SV-nodes. The latter condition can be determined by studying the event teleseismically and since we use only strike-slip events the nodes for P and SV occur along the same azimuth. All the events used in this analyses are relatively shallow, less than 15 km. The standard depth used in all the synthetics was taken as 8 km, unless stated otherwise. A map displaying the stations and events used in the direct S waveshape analyses satisfying the above criterion is given in Fig. 2 as discussed earlier.

A comparison of some of these observations with the best fitting model displaying the onset of the 400 km triplication is given in Figs. 13 and 14. Many of these events are quite small and have shorter time functions than the (1,1,1) assumed in Fig. 11, the event C2 with  $M = 5.2$  being a good example. The synthetics in these figures were computed with the WKBJ code and thus do not contain the tunnelled energy which appears as a long period onset to the mantle S phase as displayed in Fig. 15. The effect disappears at larger ranges as the S phase leaves the shadow zone boundary, in this case near  $17^\circ$ . We interpret the gradual beginning of the observed data at DAL and GOL, as primarily due to this tunneled energy. These same events as recorded at the more tectonic type stations, TUC and ALQ, have sharp onsets with little evidence of any precursors. However, the thickness of the lithosphere is likely to be highly variable across the tectonic-shield transition and given the uncertainty in attenuation effects and source durations we do not think that detailed modeling of the precursor is justified at this stage. Nevertheless, the 400 km triplication is obvious in the data and this feature alone

pattern occurred at ranges 31 to 35° in the pure tectonic model. These two arrivals, in Fig. 18, merge at larger ranges producing a strong peak. The 400 km and 600 km triplications cross near 45°. The ratio of SS to S becomes very large here but depends critically on the source duration and the precise positions of the triplications.

It appears, from this profile, that the SS phase for our model is relatively fast out to about 38°. This would indicate that the lithosphere is possibly too thick at epicentral distances less than 15°, and should grow more slowly before then, with perhaps a sharper jump at the Rocky Mountain Front. Other profiles of data along this azimuth are displayed in Grand and Helmberger (1984a). Some of these events are located far enough to the South to shift the interference pattern with respect to the stations.

There is a tendency for the ratio of S to SS amplitudes to vary somewhat from event to event. This feature of the data has not been addressed here but probably is related to small amounts of dip-slip components present in these events. Corrections for such effects would be required if the ratios were being used for attenuation measurements.

The other two models produce reasonable fits to this profile although the synthetics for SS are too slow. A comparison of two key distances is given in Fig. 19 where, as in the direct S case, the FF model appears slightly too early, particularly at  $\Delta = 36.5^\circ$ . At  $\Delta = 47.6^\circ$  the FF synthetic fits the observed waveform quite well. Note that the SFA observation is from event C3, at the California-Baja border while the observation at SCH is of the B1 event near the tip of Baja. The first leg of SS samples a zone near GOL for the former path and near JCT for the latter path. See figure 2. From many detailed comparisons between the various observations and proposed models, we reach the conclusion that substantial three-dimensional structure is present in the data. However, the RMFS model appears to be a good average two-dimensional model.

A cross-section of velocity structure with the SS ray paths appropriate for those arrivals bottoming near the 400 km discontinuity is given in Fig. 20. Note that the ray

## Discussion

The RMFS model fits a relatively large amount of travel time and waveform data and implies a rapid horizontal gradient in velocity near the Rocky Mountain Front. Exactly where the model has this sharp change relative to the surface geology is uncertain because of the averaging process discussed earlier. Nevertheless, it is interesting to compare the predicted delay time produced by this model with the observed travel time residuals, see Fig. 22. We suppose that stations BKS and GSC are near the western edge of the model and plot the relative travel time delay appropriate for vertical incidence. Correcting the data to vertical incidence would reduce the total variation by about 15% so that the over-all agreement between the model and data is quite good. Note that the most rapid changes in the data occur near stations RCD and DAL with about a 4 sec shift in travel times. These stations show considerable scatter with strong evidence of azimuthal dependence. Some of this scatter is probably caused by slab extension in the source region, Jordan (1977), and anomalies in the lower mantle, Lay (1983). However, the analysis presented here would not eliminate the possibility of horizontal gradients sharper than those suggested by RMFS and if such strong transitional boundaries exist we might expect to see some particularly interesting travel time patterns along the boundary. Note that such geologic boundaries would probably not be linear as supposed in this study. A manifestation of such structure on the character and waveshapes of recorded teleseismic signals has not been noted in the literature but, on the other hand, the data and methods required to synthesize such effects are only now becoming available.

There is a tendency for the S residuals for stations near the Eastern seaboard to become less negative. For instance, the values observed at Bermuda, BEC, appear to be only slightly smaller than predicted by JB, a result completely compatible with the ATL model presented in Fig. 1, see Grand and Helmberger (1984b).

investigations of remote regions where little direct data is available.

### **Acknowledgements**

We would like to thank Cindy Arvensen for helping with the data processing and drafting. This work was supported by the National Science Foundation Grant EAR-8306411 and by the Air Force Office of Scientific Research Grant F49620-83-C-0025. Contribution 4173, Division of Geological and Planetary Sciences, California Institute of Technology, Pasadena, California 91125.

astr., Soc., 72, 483-516.

Nuttli, O. W., (1969). Travel times and amplitudes of  $S'$  waves from nuclear explosions in Nevada, Bull. Seis. Soc. Am., 59, 385-398.

Poupinet, G. (1977). Heterogeneities du manteau terrestre deduites de la propagation des ondes de volume: implication geodynamique, These presentee a l' Universite Scientifique et Medicale de Grenoble, Grenoble, France.

Rial, J. A., Grand, S. and Helmberger, D. V., (1984). A note on lateral variation in upper mantle shear-wave velocity across the Alpine front, Geophys. J. R. astr. Soc., 77, 639-654.

Romanowicz, B. A. and Cara, M. (1980). Reconsideration of the relations between S and P station anomalies in North America, Geophys. Res. Letts., 7, 417-420.

Sengupta, M. K. (1975). The structure of the earth's mantle from body wave observations, M. S. Thesis, Massachusetts Institute of Technology, Cambridge, Massachusetts, 578 pp.

Wickens, A. J. and Buchbinder, G. G. R. (1980). S-wave residuals in Canada, Bull. Seism. Soc. Am., 70, 809-822.

arrivals.

Figure 16. Observations and synthetics displaying the interaction with the 600 km triplication. The various time histories are indicated for each synthetic.

Figure 17. Reduced travel times from observations compared with WKBJ synthetics for possible models.

Figure 18. Comparison of (SS-S) observations and synthetics. Unmarked seismograms are from event B1. Others have event numbers as in Table 1. Timing lines for SS are at same time for both data and synthetics.

Figure 19. Comparison of two example distances with corresponding synthetics.

Figure 20. Ray paths sampling the upper 400 km velocity structure as a function of lateral position.

Figure 21. Observations and synthetics. The dotted lines have been included for timing purposes.

Figure 22. Comparison of relative JB residuals with synthetics (RMFS), modified from Lay (1983). The line is dotted beyond SCP since many of these stations are near the Atlantic coast and expected to be late, see Grand and Helmberger (1984b).

Figure 23. Possible velocity cross-section, upper 400 km, from California to Greenland on the top with corresponding synthetic on the bottom. The source locations for the two observations are given below the station names, see B4 and B5 in Fig. 2. The surface bounce points for the SS phases are near Hudson's Bay and South Dakota, respectively.

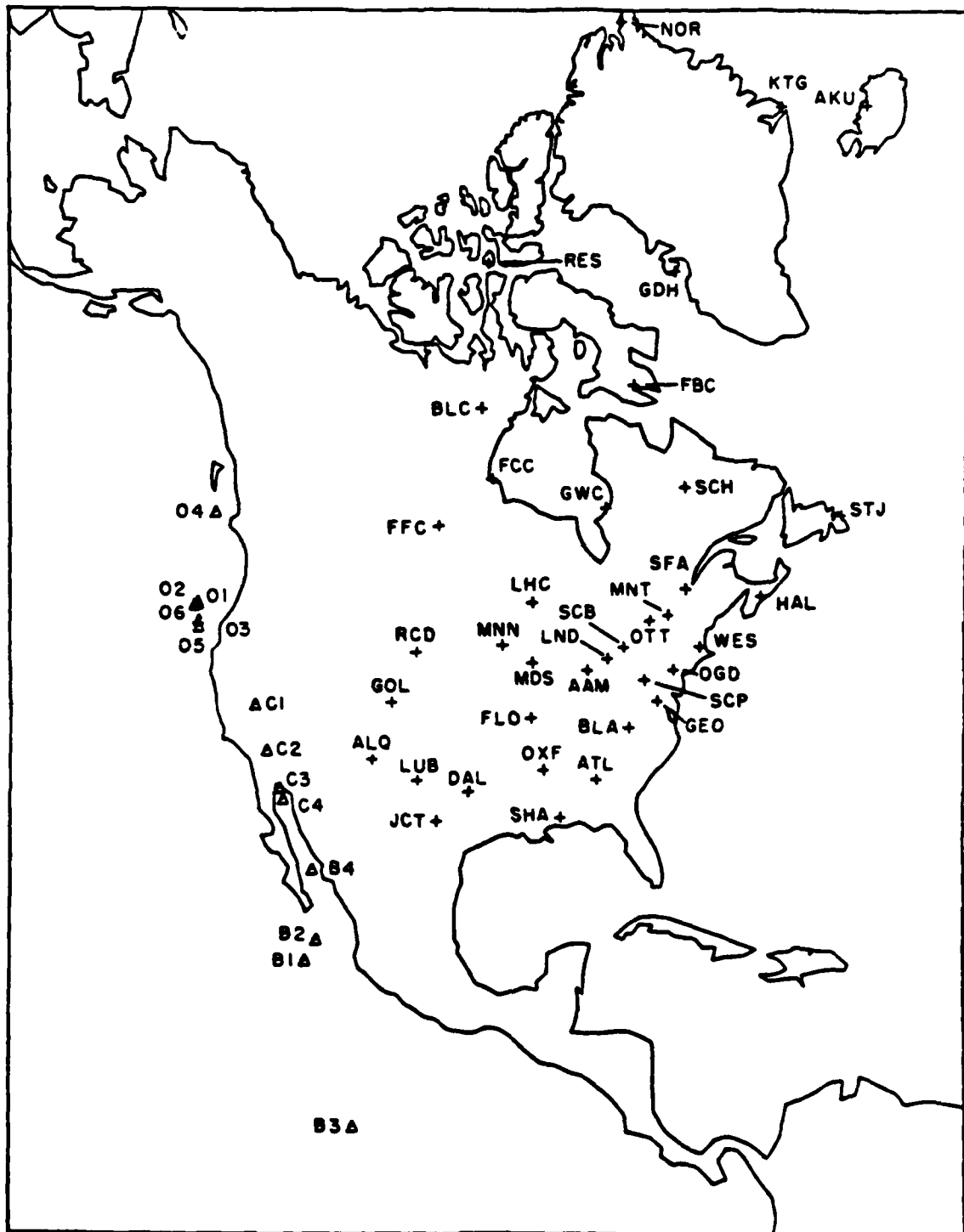


Figure 2. Map of the North American continent locating stations and events.  
See Table 1 for a list of the events and identifications.

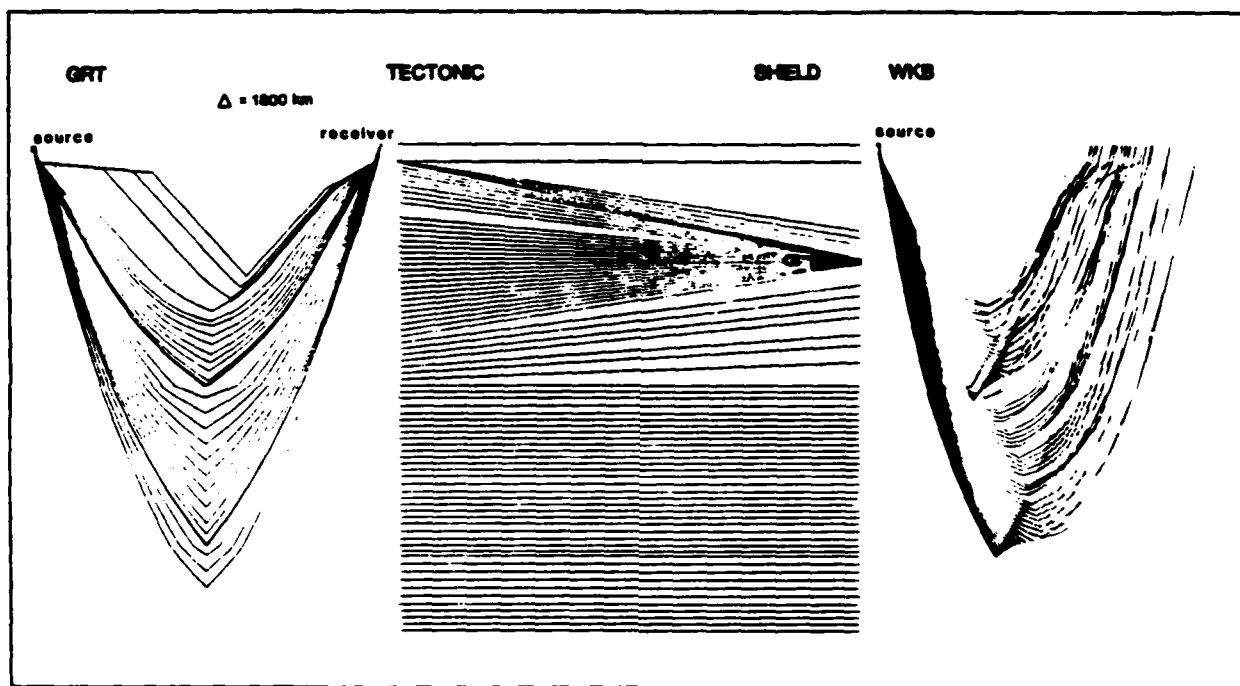


Figure 4. Example of a simple linear transition from tectonic-to-shield along with ray paths appropriate for the two methods.

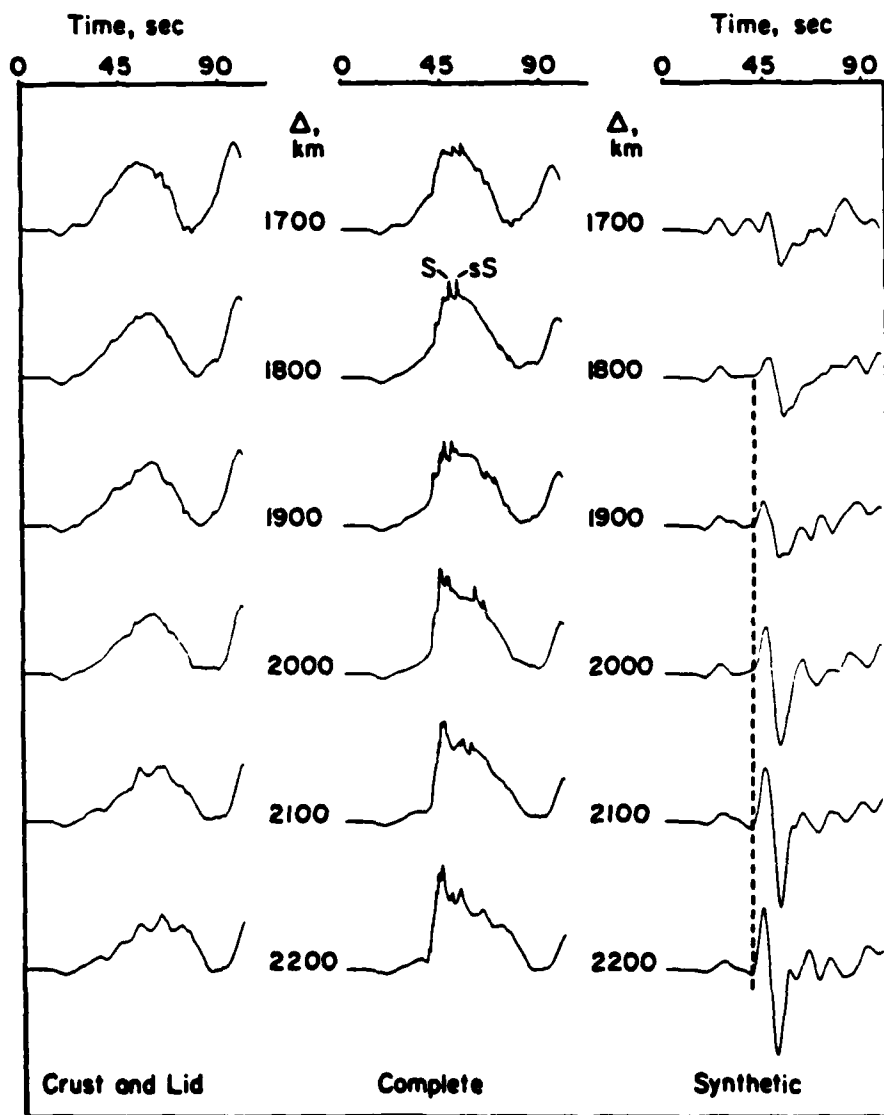
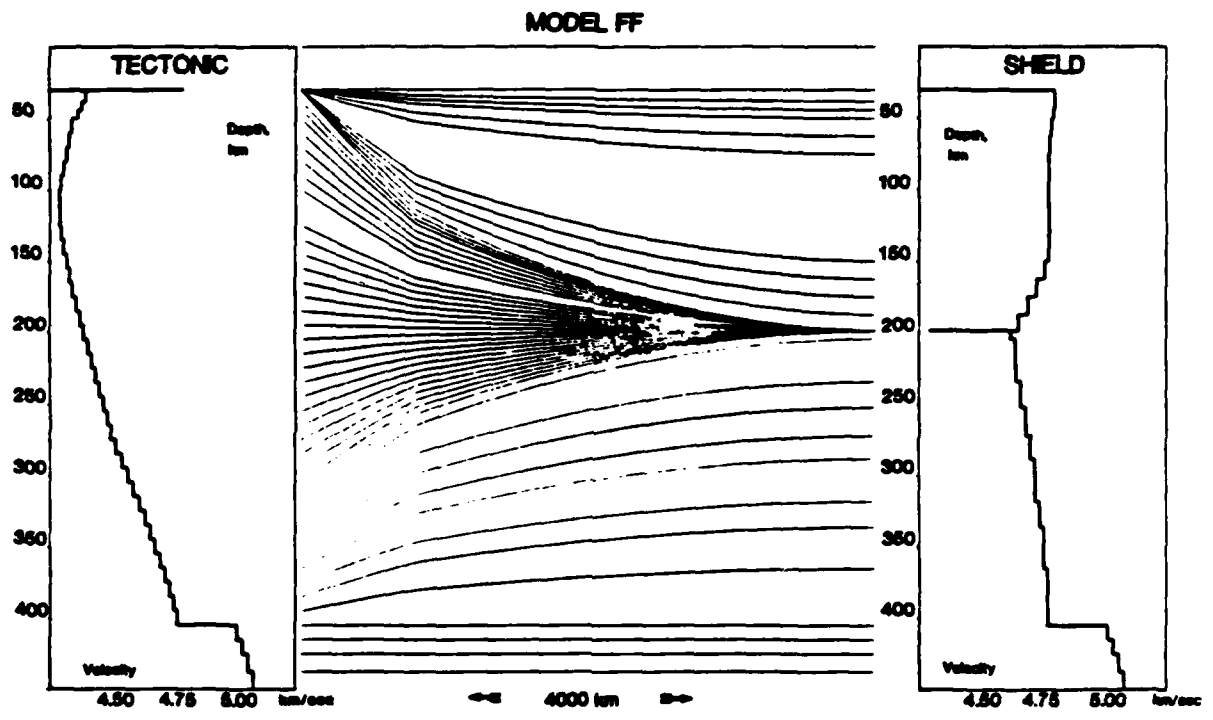
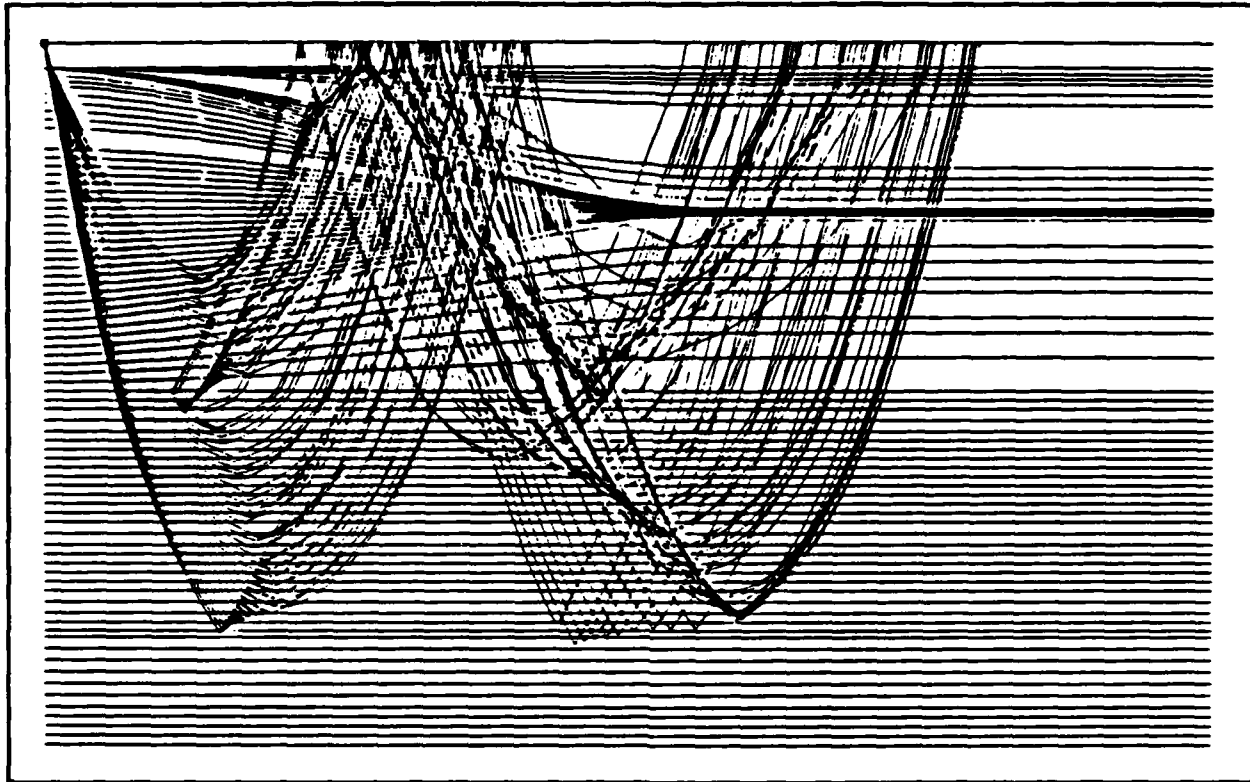


Figure 6. Step responses generated by the crust and lid on the left, complete response in the middle and associated synthetics on the right. A trapezoidal time function with duration (1,1,1) was assumed for the time history and a  $t_p^0 = 3$  was chosen for a guess at the attenuation. The dotted line indicates the mantle arrival.



**Figure 8. Model FF connecting TNA to SNA with a rapid or fast transition above and below the LVZ.**



**Figure 10. Ray paths appropriate for SS as used in the WKB analysis.**

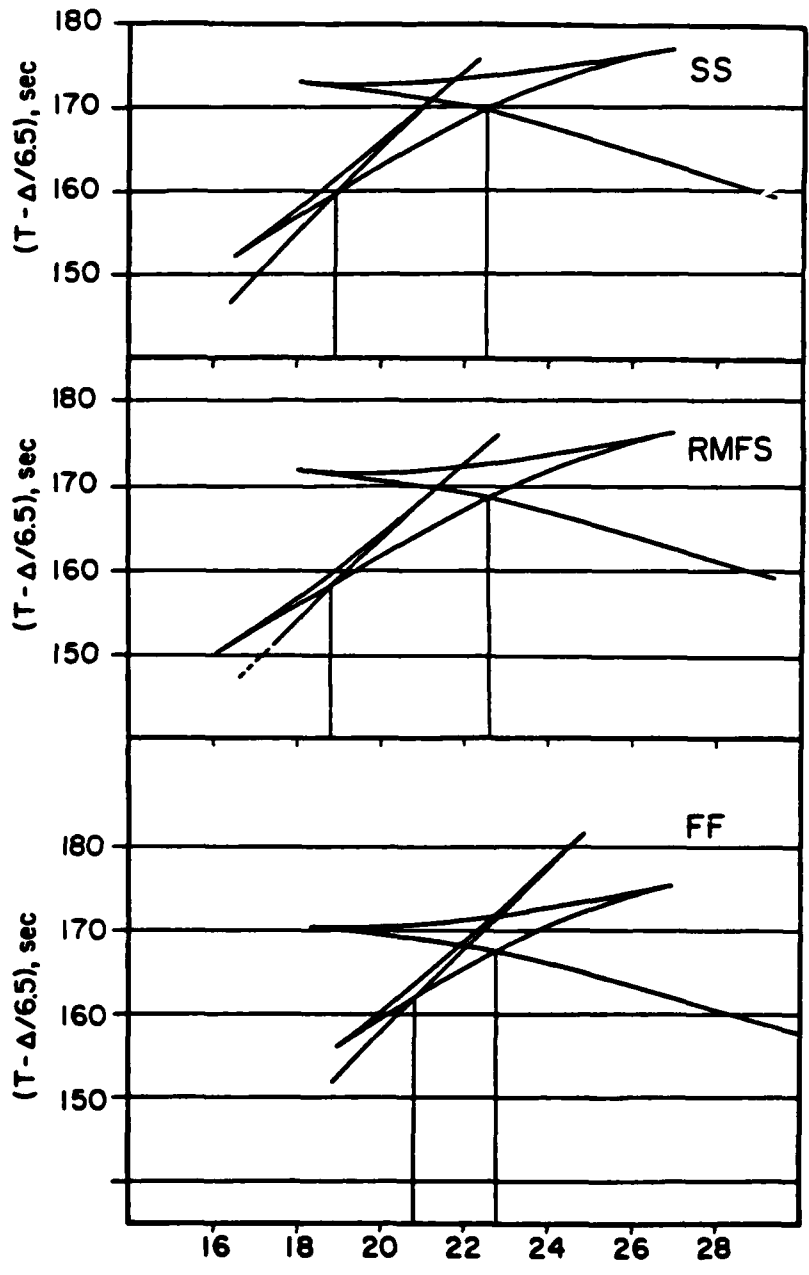


Figure 12. Triplications appropriate for the three models.

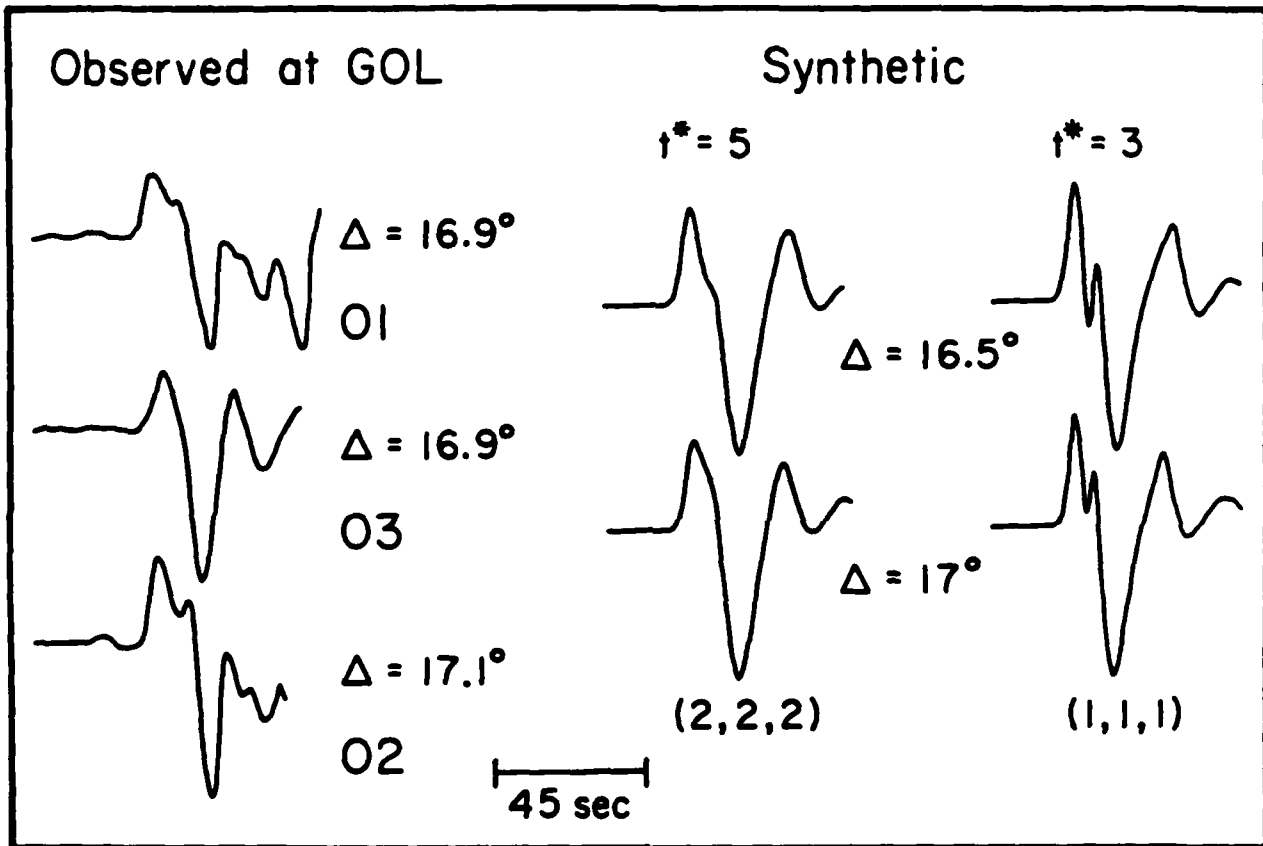


Figure 14. Observations and synthetics at GOL, Colorado for various assumptions about time histories and attenuations. Note the longer period first arrival in the data relative to the synthetics.

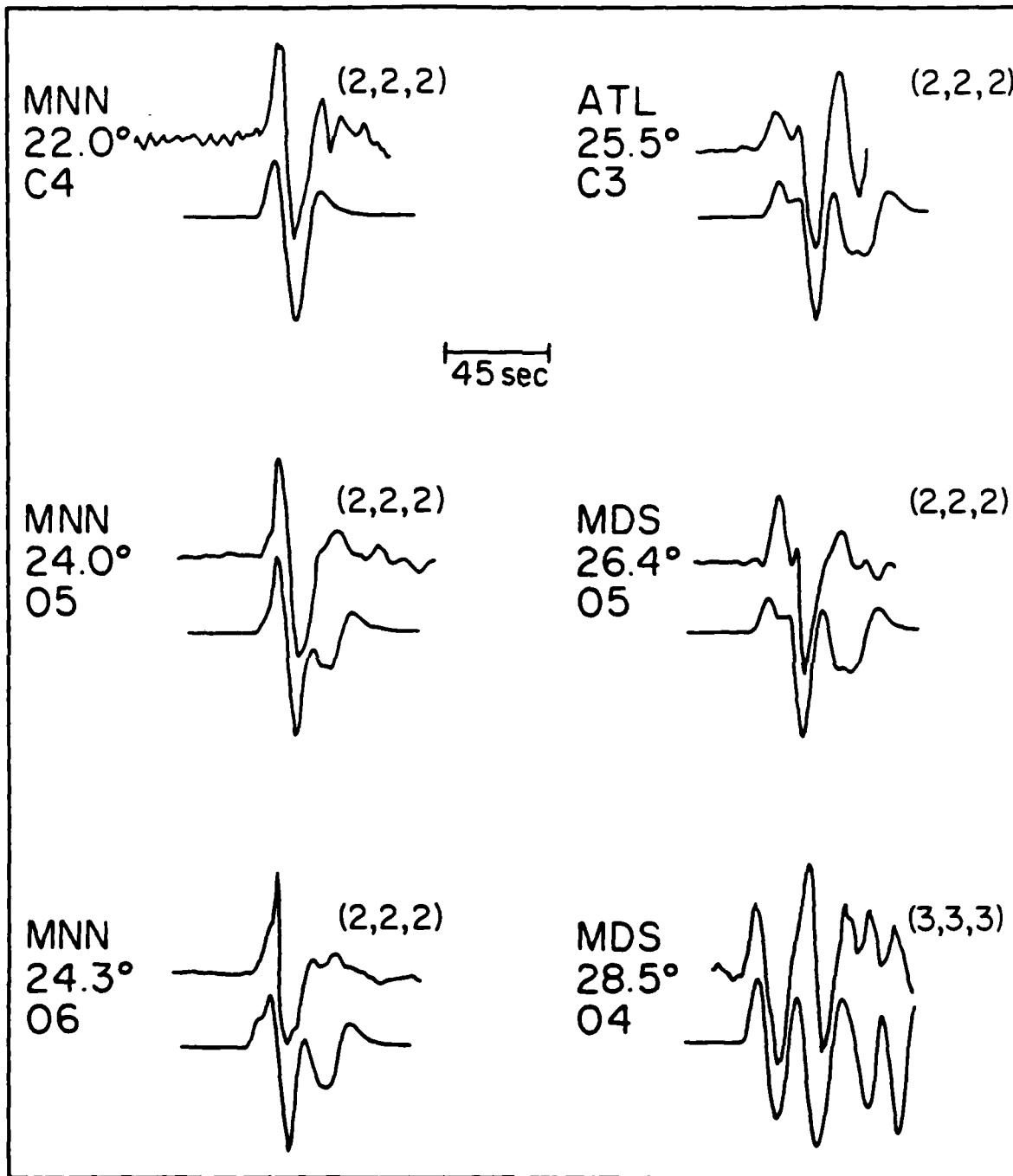


Figure 16. Observations and synthetics displaying the interaction with the 600 km triplication. The various time histories are indicated for each synthetic.

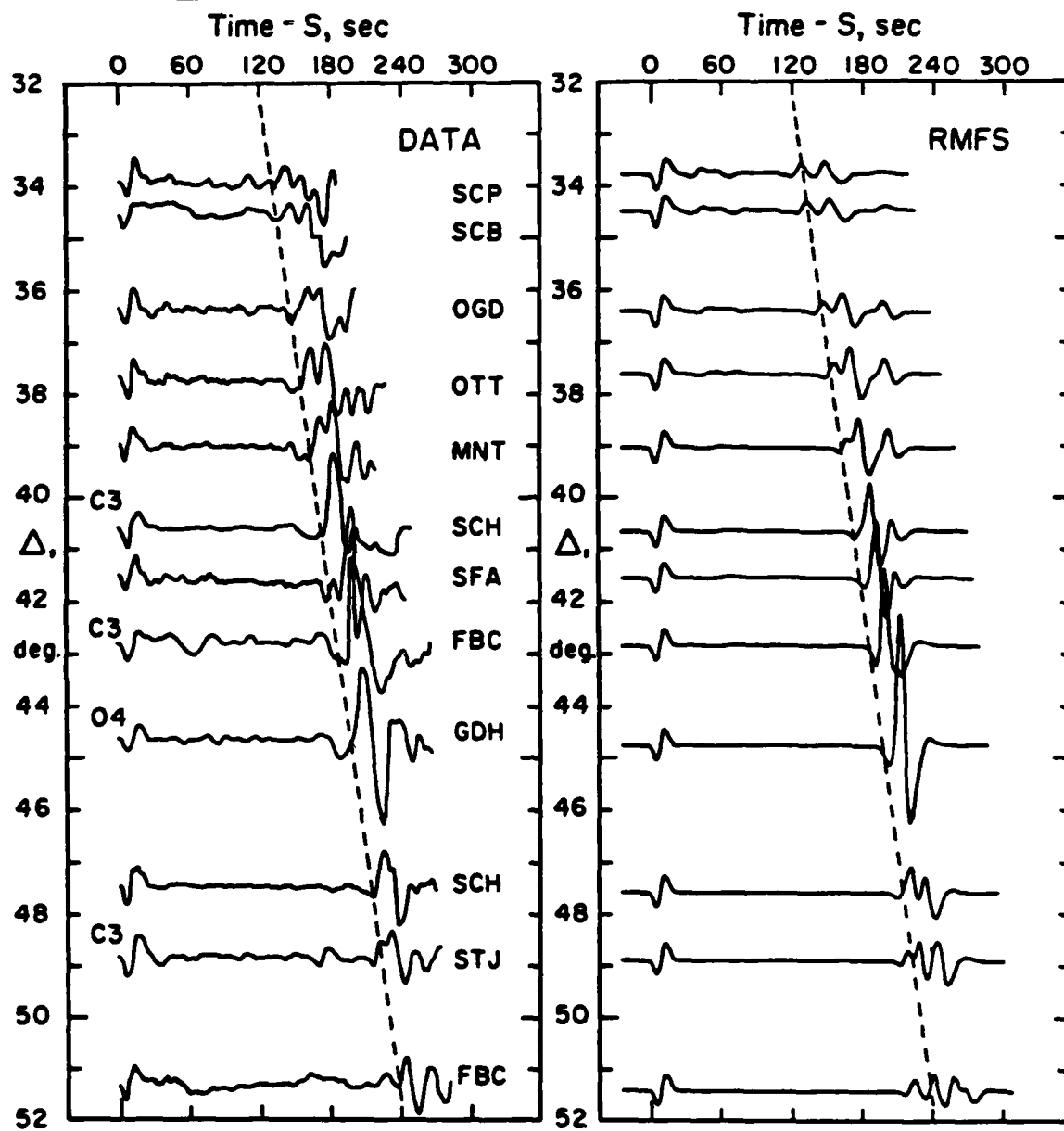


Figure 18. Comparison of (SS-S) observations and synthetics. Unmarked seismograms are from event B1. Others have event numbers as in Table 1. Timing lines for SS are at same time for both data and synthetics.

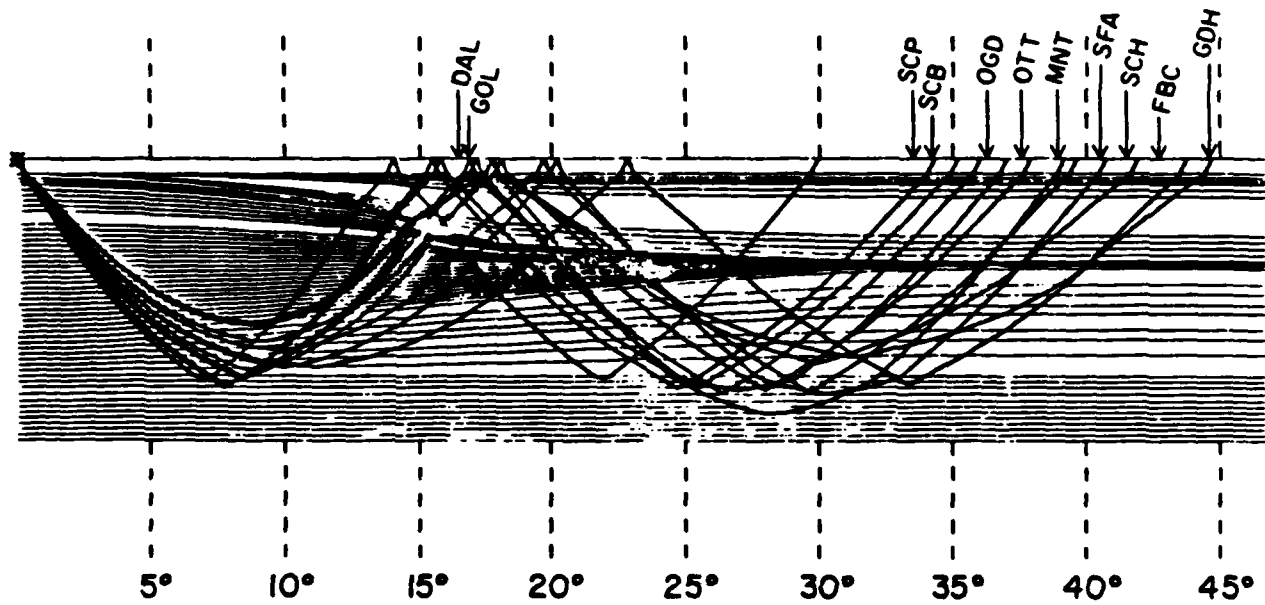


Figure 20. Ray paths sampling the upper 400 km velocity structure as a function of lateral position.

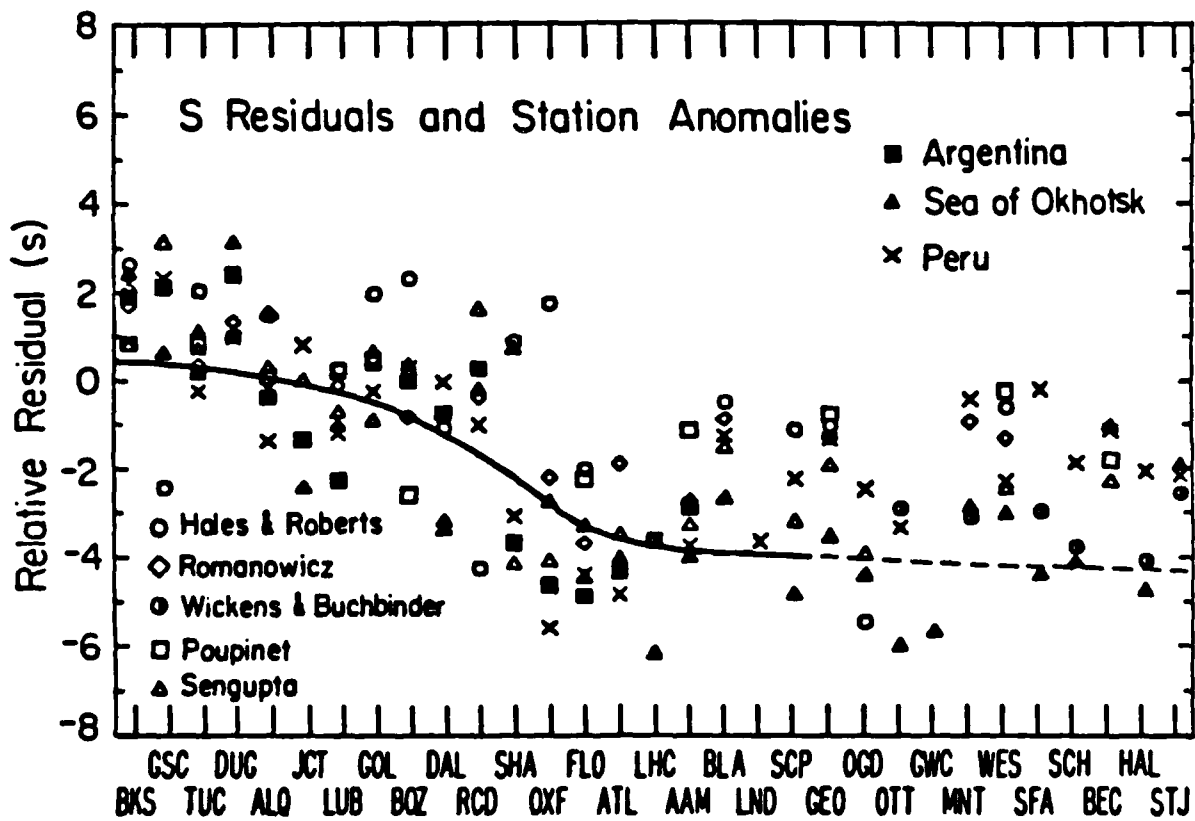


Figure 22. Comparison of relative JB residuals with synthetics (RMFS).